

# Nonresonant Exciton–Plasmon Interaction in Metal–Chalcogenide (Cu<sub>x</sub>S)/Perovskite (CsPbBr<sub>3</sub>) Based Colloidal Heterostructure

Saptarshi Chakraborty, Gauttam Dash, Subhashri Mannar, Krishna Chand Maurya, Arpan Das, Shobhana Narasimhan, Bivas Saha, and Ranjani Viswanatha\*



Cite This: <https://doi.org/10.1021/acs.jpcc.3c03331>



Read Online

ACCESS |



Metrics & More

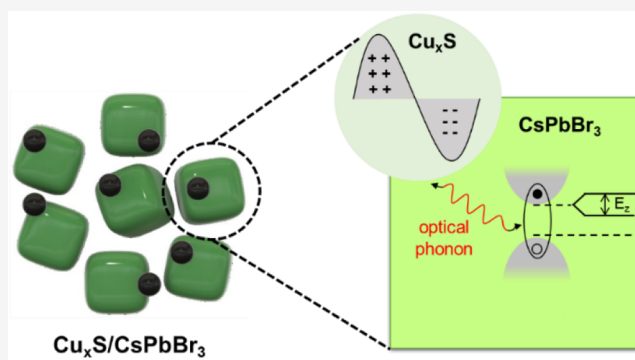


Article Recommendations



Supporting Information

**ABSTRACT:** Heterostructures often exploit exciton–plasmon coupling between two materials to enhance various optical properties, where an essential criterion is the resonant energy coupling between the two materials. Recently, however, it is shown that nonresonant exciton–plasmon interaction can take place in a single semiconductor plasmonic nanomaterial, where the plasmonic and excitonic absorptions share no energy overlap. Here, we design a colloidal heterostructure composed of plasmonic Cu<sub>x</sub>S and excitonic CsPbBr<sub>3</sub>, without any spectral overlap to study the nonresonant interaction across two different materials. The heterostructure shows different structural and optical properties such as a strained interface between the two parent components, higher Urbach energy compared to perovskite, and photoluminescence quenching that suggests possible interaction, and its magnetic circular dichroism properties show a clear signature of strong nonresonant exciton–plasmon interaction. To the best of our knowledge, this is the first demonstration of nonresonant exciton–plasmon interaction that can open new possibilities in plasmontronics.



## INTRODUCTION

Nanocrystal heterostructures, where two or more materials are blended to form a single entity, introduce new properties that pristine material lacks. One common example in recent literature reports is exciton–plasmon coupling by pairing the transition metal chalcogenides (TMC) with the metal plasmonic components.<sup>1–3</sup> This exploits the former’s large exciton binding energy with the latter’s ability to confine light in the subdiffraction limit to manipulate light–matter interaction to create single-atom lasers, all-optical switches, quantum information processing, and even Bose–Einstein condensation.<sup>2</sup> Recent examples of such heterostructures include ultrathin single-crystalline gold nanodisks on monolayers of WS<sub>2</sub>,<sup>3</sup> monolayer WS<sub>2</sub> coupled with a plasmonic gold nanorod to harvest substantial enhancement in polarized photoluminescence (PL),<sup>4</sup> and charged exciton–plasmon polaritons in a hybrid WS<sub>2</sub> monolayer–plasmonic silver nanoantenna system, where the oscillator strengths of neutral and charged excitons or polariton band gaps can be electrically tuned.<sup>5,6</sup> More complex geometries include a hexagonal boron nitride encapsulated WSe<sub>2</sub> monolayer on top of a single-crystalline silver substrate, where the tight confinement of the surface plasmon polaritons (SPPs) in the plasmonic cavity enables strong coupling between excitons and SPPs when the WSe<sub>2</sub> exciton absorption is resonant with the cavity mode, showing promise as an electroplasmonic modulator by

electrically tuning the Fermi level of the TMC monolayer.<sup>1</sup> Recently, graded colloidal CdSe/ZnS core/shell QDs also showed promise in demonstrating different regimes of coupling with plasmonic surface lattice resonance, highlighting the density-dependent transition from localized to delocalized coupling.<sup>7</sup>

It should be noted that all these examples use two important criteria to achieve the exciton–plasmon coupling—a certain physical proximity between the two components and a good amount of spectral overlap between the two bands, which enables resonance energy transfer.<sup>8</sup> The principal question we try to address here is if the exciton and plasmon can interact in the absence of the spectral overlap. The idea of this so-called “nonresonant interaction” was first conceived by Radovanovic’s group back in 2018, who discovered that electron polarization can take place in degenerately doped n-type In<sub>2</sub>O<sub>3</sub> nanocrystals (NCs) enabled by nonresonant coupling of cyclotron magnetoplasmonic modes with the exciton at the Fermi level.<sup>9</sup> In later years, the same group extended their study to

Received: May 18, 2023

Revised: July 18, 2023

understand the role of faceting in field-induced excitonic splitting by plasmon modes of TiO<sub>2</sub> NCs,<sup>10</sup> and the role of dopants in plasmon-induced carrier polarization in In<sub>2</sub>O<sub>3</sub> NCs.<sup>11</sup> Most recently, it was reported that exciton polarization induced by cyclotron motion of free carriers is a universal phenomenon in semiconductor plasmonic NCs.<sup>12</sup> However, it is noteworthy that there is a general lack of understanding of tools to study these interactions. In this work, we probe these nonresonant interactions using magneto-optics, in particular, magnetic circular dichroism (MCD) spectroscopy. These techniques rely on the modulation in the polarization direction, intensity, and phase of the incident light after its interaction with the materials.<sup>13</sup> Under a strong magnetic field, the spin degeneracy of the system is lifted, which leads to different absorption of left and right circularly polarized lights, which makes MCD a universal phenomenon observed even in achiral molecules having high spin–orbit coupling, unlike CD. One of the primary origins of MCD spectra is Zeeman splitting, which strongly depends on the total angular momentum of the system, which includes both orbital and spin contributions, where the former comes from spin–orbit coupling and the latter is from unpaired electrons in the system. Zeeman splitting of a few  $\mu\text{eV}$  can be detected through MCD, which requires a strong magnetic field (several tesla). This makes MCD a sensitive technique to detect any subtle changes in the angular momentum within the system. Since the localized surface plasmons observed in the infrared (IR) region produce additional angular momenta in the presence of magnetic field, they induce Zeeman splitting at the visible band edge which lies at the heart of these nonresonant interactions.

While all of these studies are limited to a single interface-free material, to the best of our knowledge, there are no investigations on the possibility of nonresonant interaction in heterostructures across two different compounds. In our earlier study on the In–CdO/CsPbBr<sub>3</sub> heterostructure, we showed that despite having no spectral overlap between the plasmon band of n-type In-doped CdO and excitonic band edge of CsPbBr<sub>3</sub>, the heterostructure shows higher PL quantum yield (QY) as a result of the nearly similar direct band gaps of the two, that allow the charge carrier transfer from the former to the latter's radiative recombination channel.<sup>14</sup> In this Article, we investigate the cross-platform nonresonant exciton–plasmon interaction in the heterostructure composed of excitonic CsPbBr<sub>3</sub> and plasmonic p-type Cu<sub>x</sub>S QDs. The choice of perovskite as excitonic material is rooted in its unmatched optical properties—sharp absorption edge with high absorption coefficient and high PLQY, whose changes are easily trackable, as well as its easy band gap tunability via anion exchange. We first study the synthesis and structural and optical properties of this new material Cu<sub>x</sub>S/CsPbBr<sub>3</sub> via microscopy, X-ray absorption fine structure (XAFS), absorption, and emission spectroscopies in combination with ellipsometry and first-principles density functional theory (DFT) calculations and then investigate the influence of Cu<sub>x</sub>S plasmons on the excitonic band edge of CsPbBr<sub>3</sub> under variable magnetic field via MCD spectroscopy. Our studies suggest that plasmons modulate the excitons, although the effect is weak in absence of external perturbation. Once a perturbation (magnetic field) is applied, the degeneracy of the energy states is lifted, which modifies the excitonic MCD signal in the heterostructure compared to the pristine perovskite.

## EXPERIMENTAL METHODS

**Materials.** Chemicals used in the experiments include sulfur powder, Cs<sub>2</sub>CO<sub>3</sub> (99.99%), 1-octadecene (ODE, 90%), oleic acid (OA, 90%), oleylamine (OLAm, 70%), and methyl acetate (anhydrous, 99.5%), which were used directly after purchasing from Sigma-Aldrich. Copper(II) acetate monohydrate was obtained from SDFCL, and PbBr<sub>2</sub> (98+%) was purchased from Alfa-Aesar. Hexane and toluene were purchased from Merck (Emparta). All solvents and reagents were directly used without further purification.

**Preparation of Cs-Oleate.** Cs<sub>2</sub>CO<sub>3</sub> (405 mg, Aldrich, 99.9%) was loaded into 50 mL 3-necked flask along with ODE (10 mL) and OA (1.25 mL), degassed for 1 h at 120 °C, and then heated under Ar to 150 °C until all Cs<sub>2</sub>CO<sub>3</sub> reacts with OA forming Cs-oleate. This solution was then cooled and stored in Ar environment in septum capped vials. Since Cs-oleate precipitates out of ODE at room-temperature, it was preheated to 100 °C before using it in nanocrystal synthesis.

**Synthesis of Cu<sub>x</sub>S QDs.** A 1 mmol portion of sulfur powder was dissolved in 5 mL of ODE and dried under vacuum in the presence of 5 mL of OLAm at 130 °C for 30 min before cooling to room temperature, resulting in a clear yellow solution. This solution was dried again at room temperature for an hour following the addition of 0.5 mmol of cupric acetate, and slowly heated to 200 °C. This condition was maintained for 30 min before cooling to room temperature, forming a dark green solution of Cu<sub>x</sub>S QDs. The solution was directly centrifuged at 5000 rpm for 6 min in a centrifuge machine to precipitate the particles, after which the clear supernatant was discarded, and the particles were dissolved in 8 mL ODE. Then 3 mL of this solution was used as the *solvent* for heterostructure synthesis in the next step.

**Synthesis of CsPbBr<sub>3</sub> and Heterostructures.** The undoped CsPbBr<sub>3</sub> and final step of heterostructure synthesis closely followed the method reported by Protesescu et al.<sup>15</sup> For CsPbBr<sub>3</sub> synthesis, 0.188 mmol of PbBr<sub>2</sub>, 5 mL of the ODE, 1 mL of OLAm, and 1 mL of OA were loaded into a 50 mL 3-necked flask and degassed under vacuum for 1 h at 120 °C. For heterostructure, the *solvent* containing Cu<sub>x</sub>S QDs (3 mL), OLAm (0.5 mL), OA (0.5 mL), and 0.188 mmol of PbBr<sub>2</sub> were dried and digestively ripened at the same temperature. The temperature was then raised to 120 °C, 150 °C, and 180 °C depending on the reaction after complete solubilization of PbBr<sub>2</sub> salt, and Cs-oleate solution (0.4 mL preheated to 100 °C) was quickly injected. Five seconds later, the reaction mixture was cooled by ice water bath to quench the growth of the particles.

**Isolation and Purification of QDs.** Cu<sub>x</sub>S QDs were precipitated by centrifuging the as-prepared solution at 5k rpm for 6 min in a centrifuge machine. The CsPbBr<sub>3</sub> and Cu<sub>x</sub>S/CsPbBr<sub>3</sub> QDs were washed by directly centrifuging it at 5k rpm for 10 min in a centrifuge machine, after which the supernatant was discarded and the QDs were redispersed in hexane (CsPbBr<sub>3</sub>) or toluene (Cu<sub>x</sub>S/CsPbBr<sub>3</sub>). This solution was processed in a vortex until colloidal stable and uniform sample was found. Methyl acetate was then added to this solution (three times sample volume) and centrifuged at 10k rpm for 3 min in a microcentrifuge machine. The resulting supernatant was preserved and used for further optical studies.

**Spectroscopic Characterization.** Crystal structure identification of the samples was carried out using XRD, recorded

on a Rigaku Smartlab and Bruker D8 Advanced Diffractometer using Cu  $K\alpha$  radiation. The bulk XRD data was obtained from The Materials Project database.<sup>16</sup> UV–visible absorption spectra were measured using an Agilent 8453 UV–visible spectrometer for the QDs heterostructures dissolved in toluene after dual washing. NIR absorbance spectra were recorded in a PerkinElmer Lambda 750 UV/vis/NIR spectrometer using a 60 mm integrated sphere. Steady state PL spectra were collected using the 450 W xenon lamp as the source on the FLSP920 spectrometer, Edinburgh Instruments. The absolute QY was determined using an integrating sphere from Edinburgh Instruments. Trace-metal analysis was carried out using inductively coupled plasma optical emission spectrometry (ICP-OES) on a PerkinElmer Optima 7000D ICP-optical emission spectrometer. Imaging of the QDs was done by using a JEOL JEM-2100 plus transmission electron microscope with an accelerating voltage of 200 kV. MCD studies were performed on an Oxford SO 65633 7T magnet with a Jasco 1500 CD spectrometer. Samples were drop casted on a spectrocil-B slide, and the measurements were done at 2 K temperature at variable magnetic field.

**XAFS Data Measurement and Processing.** The XAFS data were collected at the P64 beamline at PETRA III, DESY in Hamburg, Germany. All of the measurements were made in reflection geometry in fluorescence mode on thin films. X-ray energy was calibrated to 8979 and 13035 eV for Cu\_K and Pb\_L<sub>III</sub> measurements, respectively.

Data were processed using *Athena*<sup>17</sup> software plotting the EXAFS oscillation  $\chi(k)$  in wavenumber ( $k$ ) space as a function of photoelectron wavenumber  $k$  and then Fourier transforming in position ( $R$ ) space through a Hanning window for the visual representation of the bond-lengths involved in the system. After the edge energies were calibrated to the respective metal foil energies, several scans for each data were merged to get better-quality data before fitting them to theoretical standards, which were analyzed with the fitting software *Artemis*<sup>17</sup> to get quantitative information about the local environment of the NCs. Throughout the analysis, the theoretical standards to which the experimental data were fitted were generated from *FEFF6* built into *Artemis* within a cluster size of 7 Å.

**Ellipsometry Sample Preparation and Measurements.** For the preparation of samples for ellipsometry measurements, a glass slide, cleaned using hexane and acetone, was used as the substrate, on which the directly washed samples were spin-coated at three different steps, respectively, at 300 rpm for 1 min and 20 s, 500 rpm for 1 min and 30 s, and finally at 1000 rpm for 30 s. These gradually increasing angular velocities ensure a smooth film with uniform thickness for regular reflection from the surface, by minimizing surface roughness due to sample inhomogeneities. The experimental parameters Psi ( $\psi$ ) and Delta ( $\Delta$ ), connected to the Fresnel coefficients  $R_p$  and  $R_s$  for p and s polarized light via  $\frac{R_p}{R_s} = \tan \psi e^{i\Delta}$ , were performed in the reflection mode at three different angles (55°, 65°, and 75°) of incidences in J. A. Woollam Co. RC-2 ellipsometer. The experimental (Psi ( $\psi$ ), Delta ( $\Delta$ )) spectra were modeled by Gaussian oscillators (eq 1) in CompleteEASE software provided by Woollam Co. The real ( $\epsilon_1$ ) and imaginary ( $\epsilon_2$ ) parts of the dielectric function ( $\epsilon = \epsilon_1 + i\epsilon_2$ ) of the materials were extracted from the ellipsometry parameters  $\psi$  and  $\Delta$  (Figure S5) modeled respectively using Kramers–Kronig relations and Gaussian oscillators (eq 1) to provide physical insights into the systems.

The fitting summary is shown in Table S2. The imaginary part of the dielectric function ( $\epsilon_2$ ) extracted gives the real part of permittivity ( $\epsilon_1$ ). The total dielectric permittivity function can be written as,

$$\epsilon(\omega) = \epsilon_1 + i\epsilon_2 = \epsilon_\infty + Amp \left\{ \left[ \Gamma \left( \frac{E - E_{0n}}{\sigma_n} \right) + \Gamma \left( \frac{E + E_{0n}}{\sigma_n} \right) \right] + i \left[ \exp \left[ - \left( \frac{E - E_{0n}}{\sigma_n} \right)^2 \right] - \exp \left[ - \left( \frac{E + E_{0n}}{\sigma_n} \right)^2 \right] \right] \right\} \quad (1)$$

where,

$$\sigma_n = \frac{Br_n}{2\sqrt{\ln(2)}} \quad (2)$$

Here  $\epsilon_\infty$  is the high-frequency dielectric constant,  $Amp$  is the amplitude,  $E_0$  is the resonance energy,  $n$  is the number of oscillators,  $Br$  is the broadening, and  $\Gamma$  is a convergence series that produces a Kramers–Kronig consistent line shape for  $\epsilon_1$ . The real part of permittivity ( $\epsilon_1$ ) signifies the optical response of the material, and the imaginary part of permittivity ( $\epsilon_2$ ) is the optical losses due to interband, intraband transition etc.

**Computational Methods.** All calculations were performed using DFT as implemented in the Quantum ESPRESSO package.<sup>18</sup> The interactions between the valence electrons and ionic cores were described using norm-conserving pseudopotentials.<sup>19</sup> The exchange correlation functional was treated using a Generalized Gradient Approximation of the Perdew–Burke–Ernzerhof (PBE-GGA) form.<sup>20</sup> The Kohn–Sham wave functions and the corresponding charge densities were expanded in plane-wave basis sets having cut-offs of 80 and 320 Ry, respectively. Brillouin zone sampling was done using an  $8 \times 8 \times 8$  Monkhorst–Pack mesh,<sup>21</sup> along with Marzari–Vanderbilt cold smearing<sup>22</sup> of width 0.001 Ry. The optical properties of CsPbX<sub>3</sub> (X: Cl, Br) were calculated using the *epsilon.x* postprocessing routine that is a part of the Quantum ESPRESSO package.<sup>18</sup> The imaginary part of the dielectric tensor  $\epsilon_2$ , was calculated using the Drude–Lorentz model, using the formula:<sup>23</sup>

$$\epsilon_{2,\alpha\beta}(\omega) = \frac{8\pi e^2}{\Omega N_k m^2} \sum_{n \in V} \sum_{n' \in C} \sum_k \frac{\hat{M}_{\alpha,\beta}}{E_{k,n'} - E_{k,n}} \frac{\Gamma \omega f(E_{k,n})}{[(\omega_{k,n'} - \omega_{k,n})^2 - \omega^2]^2 + \Gamma^2 \omega^2} \quad (3)$$

where  $\alpha, \beta$  run over the Cartesian directions  $x, y, z$ .  $\Omega$  is the volume of the unit cell,  $n$  and  $n'$  index the VB and CB respectively,  $k$  indexes the wave-vectors sampled in the Brillouin zone,  $N_k$  is the total number of such  $k$ -points,  $\omega$  is the frequency,  $E_{k,n}$  are the Kohn–Sham eigenvalues,  $E_{k,n'} - E_{k,n}$  are transition energies,  $e$  and  $m$  are electron's charge and mass, respectively,  $\Gamma$  is the interband broadening parameter, and  $f(E_{k,n})$  is the Fermi–Dirac distribution function that accounts for the occupation of the bands. Here,  $\hat{M}_{\alpha,\beta}$  is the squared

matrix element of the momentum operator. Only direct transitions are considered, and contributions from the nonlocal part of the pseudopotential are neglected. The value of  $\Gamma$  was set to 0.2 eV (to identify the peaks due to individual transitions) or 0.4 eV (to compare with the experimental data).

## RESULTS AND DISCUSSIONS

The heterostructures were synthesized via a two-step colloidal process mediated by digestive ripening, as shown in Figure 1.

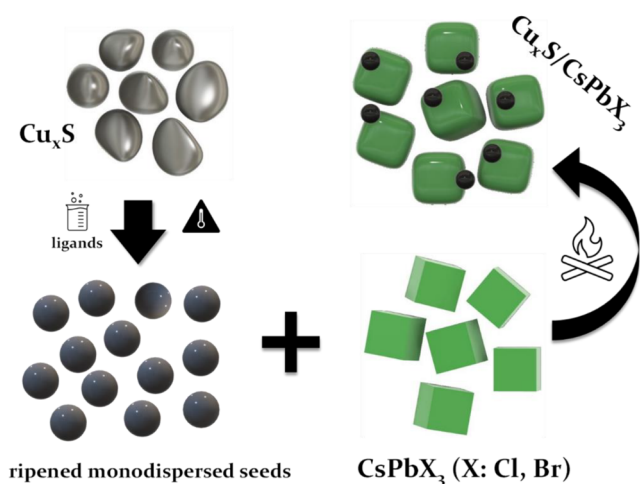


Figure 1. Schematic for two-step heterostructure formation.

Briefly, we synthesized Cu-deficit plasmon active  $\text{Cu}_x\text{S}$  QDs following an earlier report<sup>24</sup> wherein Cu-acetate was added to degassed S powder and heated to the required temperature. The detailed procedure is described in the Experimental Section. As revealed by transmission electron microscopy (TEM) (Figure S1a and S1b), as-synthesized  $\text{Cu}_x\text{S}$  QDs are mostly uniform in size with an average diameter of 13.5 nm. Interplanar distance ( $d$ ) analysis from high-resolution TEM (HRTEM) images confirms that the particles are mostly composed of the plasmon active CuS hexagonal  $P6_3/mmc$  phase (Materials Project ID (MPID): mp-504). The presence of a clear LSPR signal in the near-infrared region in the final product (Figure S1c) adheres to our requirement of having a plasmonic material as a starting component of heterostructure synthesis, where no overlap is expected with the exciton bands of perovskite. Subsequently, the obtained  $\text{Cu}_x\text{S}$  QDs were dissolved in 1-octadecene (ODE) after washing, along with the necessary precursor ( $\text{PbBr}_2$  salt) and ligands. The temperature was successively raised to the required values (120–180 °C) and after the injection of Cs-oleate, the solution was cooled with an ice bath, similar to the literature method (see Experimental Section).<sup>15</sup> The resulting particles were dissolved in hexane or toluene after direct centrifugation and used for further study. It can be noted that  $\text{Cl}^-$  based heterostructures can be obtained in a manner similar to the  $\text{PbCl}_2$  precursor, which have identical structural and optical properties. Thus, this article will only focus on  $\text{Br}^-$  based compounds.

The best synthesis temperatures for all the compounds were obtained by varying the temperatures at 180 °C, 150 °C, and 120 °C. For future reference, the samples thus obtained will be termed Br- $T$ , where  $T$  corresponds to the synthesis temperature. Br-120 displays particle agglomeration (Figure S2), but both Br-180 and Br-150 were found to be of good quality and

suitable for studies. As can be seen in Figures 2a and S3 (HRTEM image), particles from the Br-150 sample have “cube-dot” architecture, that is, a 3–4 nm dot attached to a bigger cube, similar to previously reported metal chalcogenide-based<sup>25</sup> and oxide-based perovskite heterostructures,<sup>14</sup> in contrast to the regular cube-shaped  $\text{CsPbBr}_3$  particles (Figure 2b). It should be noted that a number of reports demonstrated dots over pristine halide perovskite cubes, whose origin was traced to the degraded  $\text{Pb}^{(0)}$  nanoparticles formed with the long exposure time of X-ray.<sup>26</sup> To avoid this degradation, the HRTEM images were collected at a low voltage of 200 kV and the particles were exposed to radiation for a short amount of time. The imaging conditions were identical with both  $\text{CsPbBr}_3$  and  $\text{Cu}_x\text{S}/\text{CsPbBr}_3$ , and despite that, *only* the latter shows a cube-dot architecture, while the former comes in the simple cube. Instead, the interplanar distance analysis from the HRTEM images suggests that the dots are composed of a hexagonal CuS phase, whereas the cubes *primarily* show the presence of  $\text{CsPbBr}_3$  phase, similar to the earlier observations (Figure S3).<sup>14</sup> Notably, the perovskite phases change to orthorhombic  $Pnma$  (MPID: mp-567629) from their pristine cubic  $Pm3m$  phase. The phase transformation is corroborated via X-ray diffraction (XRD) patterns of the heterostructures in Figure 2c and 2d, which show twin peaks, particularly at small angles ( $\sim 15^\circ$ ). The asymmetric broadening and a small shift in the peak position at higher angles after zero error correction further suggest the heterostructure formation. Since some peaks are present in both parent  $\text{CsPbBr}_3$  and  $\text{Cu}_x\text{S}$  phases (marked with diamonds in Figure 2c), their origin is ambiguous and can originate from either one.

An interface between the cube and the dot is clearly imaged in Figure S3—The two entities are chemically bonded, distorting the cube edge. To understand the nature of the interface between the cube and the dot, we compare the various bond lengths obtained through XAFS fittings of the  $\text{Pb}_{\text{L}_{\text{III}}}$  edges. Figure 3a shows the magnitude of the Fourier transformed data of  $\text{CsPbBr}_3$  and  $\text{Cu}_x\text{S}/\text{CsPbBr}_3$ , suggesting a reduction in the dominating interatomic distance.  $\text{CsPbBr}_3$  was modeled via the theoretical paths generated from the cubic phase of the same (Figure 3b), whereas the heterostructure’s data could be well modeled via the orthorhombic phase of  $\text{CsPbBr}_3$  as suggested by XRD, corroborating the phase transformation (Figure 3c). Our analysis shows that the  $\text{Pb}-\text{Br}$  bond length is shortened by  $\sim 2.5\%$  in the heterostructure compared to that of its parent  $\text{CsPbBr}_3$  (Table S1). Although not obtainable from the  $\text{Cu}_{\text{K}}$  edge fits because of the indeterminacy of the exact  $\text{Cu}_x\text{S}$  phase, Figure 3d clearly shows a similar reduction in the average  $\text{Cu}-\text{S}$  bond length in the heterostructure compared to the same for the parent  $\text{Cu}_x\text{S}$ . The interface between  $\text{Cu}_x\text{S}$  and  $\text{CsPbBr}_3$  is thus *strained*, generated by the presence of two compounds on other sides of the interface, leading to a compression of the lattice. This observation strongly suggests heterostructure formation since the bond length is a fundamental quantity unique to a pair of ions.

Figure 4a shows the optical properties of the heterostructures. The absorption spectra of the heterostructure precipitated from acetone have two components—an excitonic absorption originating from the  $\text{CsPbBr}_3$  phase, similar to the pristine perovskite (2.4 eV), and a plasmon band arising from  $\text{Cu}_x\text{S}$  (peak centered around 1.06 eV), with no overlap between the excitonic visible band with the plasmonic NIR one. Heterostructure formation as opposed to a physical

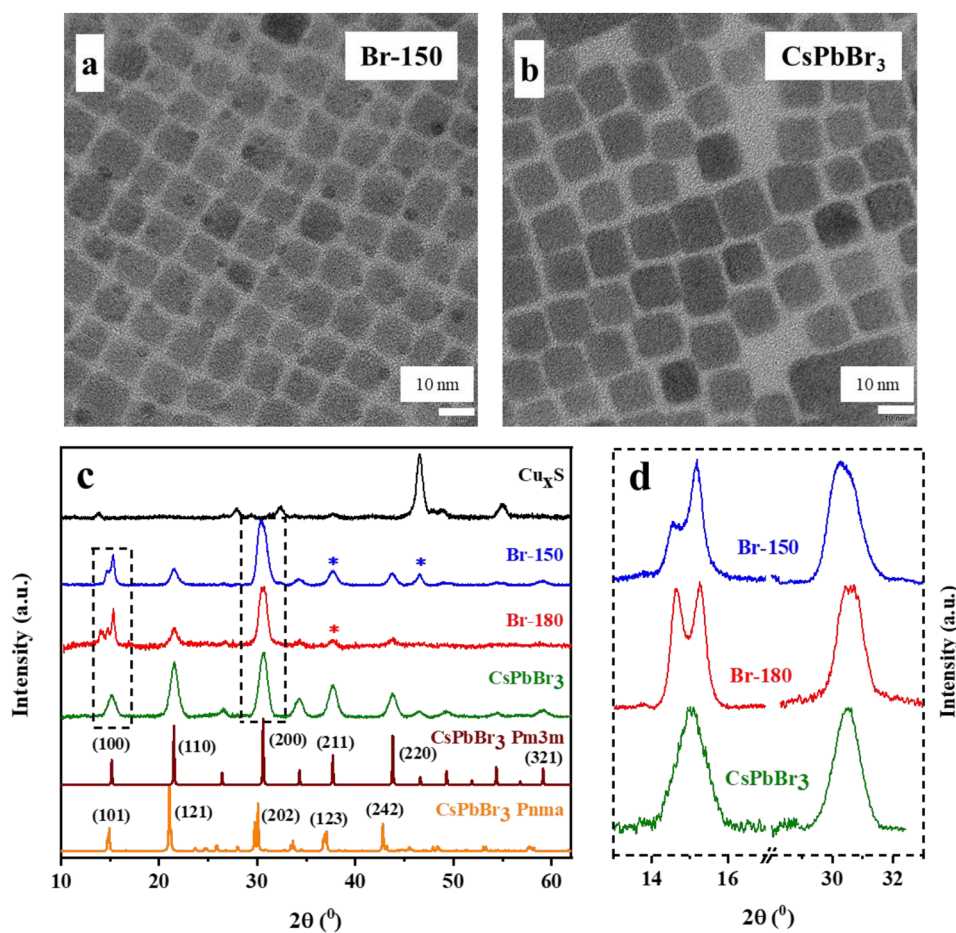


**Figure 2.** Transmission electron microscope images of (a)  $\text{Cu}_x\text{S}/\text{CsPbBr}_3$  and (b) pristine  $\text{CsPbBr}_3$ . (c) XRD patterns of  $\text{Cu}_x\text{S}/\text{CsPbBr}_3$  along with the bulk parent phases. (d) Longer scan prominently reveals peak splitting for lowest angle peaks, suggesting cubic to orthorhombic phase transformation; inhomogeneous broadening of the peak around  $32^\circ$  in case of heterostructures suggests phase change and/or lower size.

mixture was confirmed using selective precipitation with the appropriate antisolvents. It was observed that  $\text{Cu}_x\text{S}$ ,  $\text{CsPbBr}_3$  and their heterostructure respectively precipitated from methanol, methyl acetate, and acetone maintained their respective absorption spectra (Figure S4). From the absorption spectrum, although there is no sign of interaction between the components, the same of the heterostructure shows an extended absorption edge below the excitonic band gap of the material, known as the Urbach tail<sup>27–32</sup>. Although this feature can arise from scattering due to size polydispersity of the sample, TEM images of the heterostructure showed highly monodispersed QDs (see Figure 2a). In contrast, this inherent property arises from the amount of intrinsic, atomic, or electronic disorder present in the system, where the involvement of phonons in the absorption process is found to be responsible in some cases.<sup>31</sup> Hence, to quantify the disorder, we calculated the Urbach energy ( $E_U$ ) from the slope of the absorption edge following Urbach's rule, which, in logarithmic form, reads,<sup>30,32</sup>

$$\ln \alpha(E) = \sigma(T) \frac{E - E_0}{k_B T} + \ln \alpha_0 \quad (4)$$

where  $\alpha(E)$  is the absorption coefficient as a function of the incident photon energy  $E$ ,  $E_0$ , and  $\alpha_0$  are the characteristic parameters of the material,  $\sigma(T)$  is the steepness parameter, and  $k_B$  is the Boltzmann constant.  $E_U$  is defined as  $(k_B T)/\sigma(T)$

<sup>30,32</sup> The Urbach energy ( $E_U$ ) for heterostructures ( $>140$  meV) is found to be higher than that for pristine  $\text{CsPbBr}_3$  ( $\sim 38$  meV). This value for pristine  $\text{CsPbBr}_3$  matches with that reported in the literature (32 meV).<sup>30</sup> The photoluminescence quantum yield (PLQY) of the heterostructure, excited at 3.1 eV (405 nm), is found to be severely quenched, as shown in Figure 4a. This is consistent with the heterostructure formation<sup>33–36</sup> where the primary governing mechanism is identified to be resonance energy transfer (RET). Since there is hardly any band overlap between the plasmonic band of  $\text{Cu}_x\text{S}$  and the excitonic band of  $\text{CsPbBr}_3$ , the quenching is likely due to the charge transfer across the interface, which can neither be ruled out nor proven based solely on the steady-state measurements and remains beyond the scope of this work. Taken together, these are some of the preliminary hints that despite having no spectral overlap between the exciton and plasmon bands, the electronic structure can be modified, where optical phonons might play a role.

Steady-state absorption often does not resolve high energy transitions or is masked by solvent absorption. Hence, we used variable angle spectroscopic ellipsometry throughout the UV–visible and NIR range to locate the various transitions and first-principles DFT calculations to understand the origin. The imaginary part of the dielectric function  $\epsilon_2$ , that is proportional to the absorption coefficient of the system was modeled using DFT to describe the experimentally observed absorption

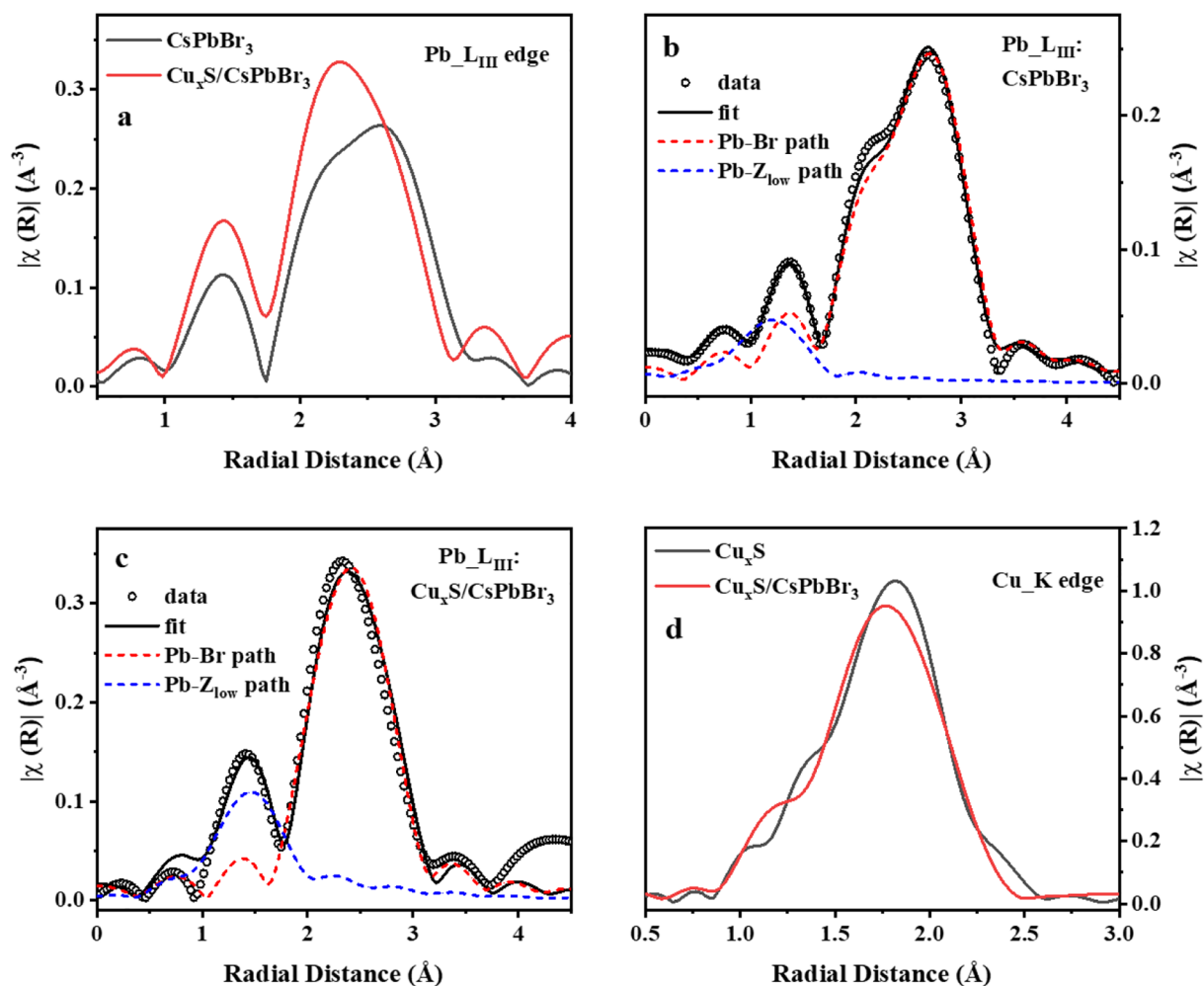


**Figure 3.** (a) Magnitude of Fourier-transformed XAFS spectra of  $\text{CsPbBr}_3$  and  $\text{Cu}_x\text{S}/\text{CsPbBr}_3$  for the Pb  $L_{III}$  edge shows a reduction in the average Pb-Br bond length. Magnitude of Fourier-transformed XAFS spectra (hollow black circles) and fittings of Pb  $L_{III}$  edge (black lines) along with the theoretical paths for (b)  $\text{CsPbBr}_3$  and (c)  $\text{Cu}_x\text{S}/\text{CsPbBr}_3$ . (d) Magnitude of Fourier-transformed XAFS spectra of  $\text{CsPbBr}_3$  and  $\text{Cu}_x\text{S}/\text{CsPbBr}_3$  for the Cu  $K$  edge shows a reduction in the average Cu-S bond length.

spectra. As shown in Figure 4b,  $\text{CsPbBr}_3$ 's  $\epsilon_2$  spectrum (red curve) is similar to its absorption spectrum, where the band-edge transition around 2.55 eV (marked as  $E_a$ ) can be clearly identified. To enable a fair comparison between theory and experiment,  $\epsilon_2$  was theoretically calculated with two different values of the interband broadening parameter  $\Gamma = 0.2$  and 0.4 eV (blue and green curves, respectively, in Figure 4b) and compared with the experimentally measured  $\epsilon_2$  (red curve). The reason for introducing two values of  $\Gamma$  is to observe the individual transitions that are not resolved by the experiment and also to be able to directly compare with the experiment. Excellent agreement between theory and experiment is obtained for both the shape and the width of the curve. The possible transitions were extracted from the second-derivative spectra of  $\epsilon_2$  using the method of critical point (CP) analysis.<sup>37,38</sup> The origin of the transitions was determined from the band structure of  $\text{CsPbBr}_3$  (Figure 4c and Table 1).  $E_a$  in both cases corresponds to the excitonic band-edge transitions ( $R \rightarrow R$ ); the rest originates from the transitions to the conduction band from different states in the valence band. We also note that the minimum in the second derivative of  $\epsilon_2$  corresponding to  $E_b$  for  $\text{CsPbBr}_3$  is rather broad and flat, and therefore a particularly large error bar is associated with the

reported value of 3.25 eV. As a result, there is a considerable uncertainty in the value of  $E_b$  and it is therefore also possible that it arises from  $M \rightarrow M$  transitions, as claimed in a previous report.<sup>39</sup> Also noteworthy is that the points  $C_a$ ,  $C_b$ , and  $C_c$  are not high symmetry points in the Brillouin zone but correspond to points where the band structure has inflection points. The projected atomic orbital contributions suggest that the top of the valence band comprises of primarily Br-4p orbitals while the bottom of the conduction bands mainly arise from the Pb-6p states throughout the Brillouin zone, except in the vicinity of the zone-center  $\Gamma$ , where Cs-6s orbitals contribute more. Thus, the orbital involvement in all the direct transitions is Br-4p  $\rightarrow$  Pb-6p for all  $k$ -points, except in the neighborhood of the  $\Gamma$  point where a Br-4p  $\rightarrow$  Cs-6s transition takes place. Figure 4d shows the experimentally obtained  $\epsilon_2$  for  $\text{Cu}_x\text{S}/\text{CsPbBr}_3$  along with its plasmonic and excitonic parents, where the LSPR and band-edge transitions can be distinctively identified within the precision of the model, similar to their absorption spectra. The CP analysis points out that except for the plasmon bands originating from  $\text{Cu}_x\text{S}$ , the high energy transitions in the heterostructure originate from its halide perovskite parent (Table S3).

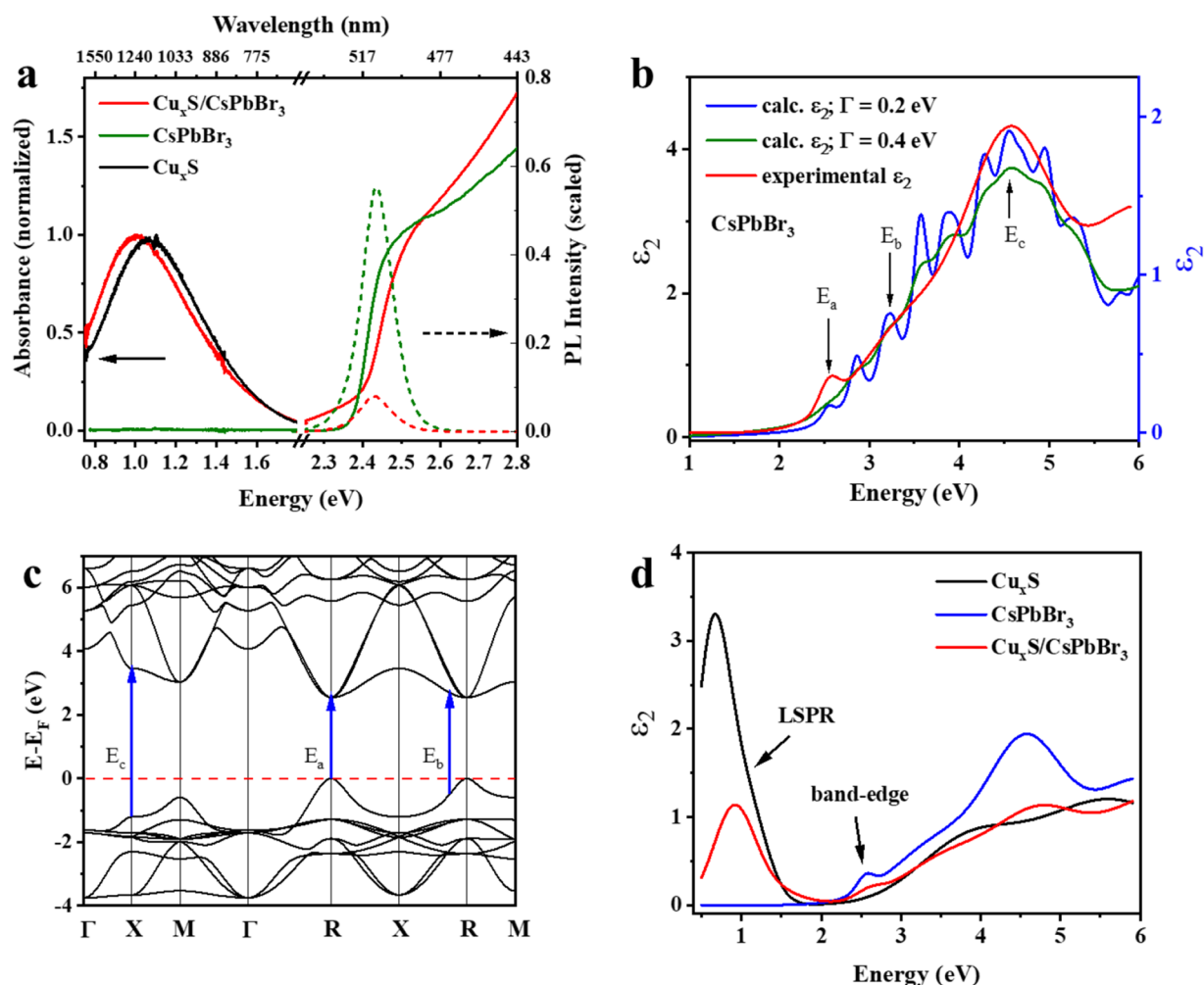


**Figure 4.** Excitonic and plasmonic absorption (solid lines) of  $\text{Cu}_x\text{S}/\text{CsPbBr}_3$  along with those of parents  $\text{Cu}_x\text{S}$  and  $\text{CsPbBr}_3$ . The PL (dashed lines) of  $\text{Cu}_x\text{S}/\text{CsPbBr}_3$  quenches compared to that of pristine  $\text{CsPbBr}_3$ . (b) Imaginary part of the dielectric function ( $\epsilon_2$ ) of  $\text{CsPbBr}_3$  obtained from ellipsometry measurements (red curve, right y axis) and DFT calculations (blue and green curves, left y axis). The blue and green curves were computed using broadening parameter  $\Gamma = 0.2$  and  $0.4$  eV, respectively. (c) Calculated and corrected band structures of  $\text{CsPbBr}_3$ . The allowed direct transitions in part b are marked as  $E_Y$  (Y: a, b, c). (d) Imaginary part of the dielectric function ( $\epsilon_2$ ) of  $\text{Cu}_x\text{S}/\text{CsPbBr}_3$  heterostructure along with the parent  $\text{CsPbBr}_3$  and  $\text{Cu}_x\text{S}$  closely resembles the materials' directly measured absorption spectra.

**Table 1. Optical Transitions in  $\text{CsPbBr}_3$  from Experiment and Theory**

expt. peak	expt. energy (eV)	transition (calc.)	calc. energy (eV)	orbitals involved
$E_a$	2.55	$R \rightarrow R$	2.55	$\text{Br-4p} \rightarrow \text{Pb-6p}$
$E_b$	3.25	$C_b \rightarrow C_b$	3.23	$\text{Br-4p} \rightarrow \text{Pb-6p}$
$E_c$	4.56	$X \rightarrow X$	4.56	$\text{Br-4p} \rightarrow \text{Pb-6p}$

Although indirect signature of nonresonant exciton–plasmon interaction was observed from the optical properties of the heterostructure, it does not provide a direct proof of the same. We study the effect of external perturbation like a magnetic field on the optical properties to observe these signatures. MCD properties of  $\text{Cu}_x\text{S}$ ,  $\text{CsPbBr}_3$ , and  $\text{Cu}_x\text{S}/\text{CsPbBr}_3$  at a temperature of 2 K and 5 T magnetic field are shown in Figure 5a along with the linear absorption spectra at that temperature for reference. The derivative feature of the excitonic band edge feature arising from the  $1s_c-1s_h$  transition is observed for both  $\text{CsPbBr}_3$  and  $\text{Cu}_x\text{S}/\text{CsPbBr}_3$  and is a result of the field induced differential absorption of left and

right circularly polarized light.<sup>40</sup> This is the  $R \rightarrow R$  transition obtained from our calculation ( $E_a$  in Figure 4c). We observed about a 10-fold reduction in the MCD amplitude in the heterostructure in comparison to parent perovskite (Figure 5a), while no detectable MCD signal was observed for pristine  $\text{Cu}_x\text{S}$  in the visible region. In addition, we also observe a reversal of sign, possibly due to the change in the nature of carriers.<sup>12</sup> It can be noted that this change in the MCD spectra is fundamentally different from the earlier works, where the excitonic band-edge and plasmonic absorptions belong to the same materials, whereas here we probe the perovskite's band edge, which shows MCD amplitude reduction upon heterostructure formation.

Despite having no visible shift in the optical band-edge absorption, the zero crossing of the MCD spectra is shifted toward lower energy by 46 meV for the heterostructure. Moreover, the splitting of the peaks (energy difference between MCD peaks) is much lower in the heterostructure (37 meV) compared to that in the pristine perovskite (73 meV). Given the fact there is no resonant coupling between  $\text{CsPbBr}_3$  and  $\text{Cu}_x\text{S}$ , this modification in the electronic structure

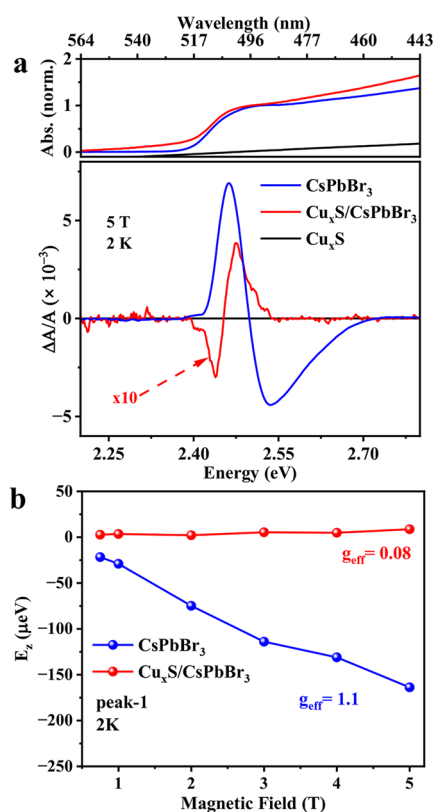


**Figure 5.** (a) Excitonic band-edge absorption (top panel) and MCD spectra (bottom panel) taken at a 5 T magnetic field and 2 K temperature for Cu<sub>x</sub>S, CsPbBr<sub>3</sub>, and Cu<sub>x</sub>S/CsPbBr<sub>3</sub>. The MCD spectra of Cu<sub>x</sub>S/CsPbBr<sub>3</sub> (red curve) are multiplied by 10 for clarity. (b) Calculated Zeeman energy for the lower energy peaks (at 2.46 eV for CsPbBr<sub>3</sub> and at 2.44 eV for Cu<sub>x</sub>S/CsPbBr<sub>3</sub>) as a function of magnetic field for Cu<sub>x</sub>S/CsPbBr<sub>3</sub> and CsPbBr<sub>3</sub>.

of the heterostructure could be due to nonresonant plasmon absorption of Cu<sub>x</sub>S. To get a quantitative measure of the splitting, Zeeman energy ( $E_z$ ) was calculated for the excitonic peak following standard literature method.<sup>41</sup> As shown in Figure 5b, the Zeeman energy for the heterostructure calculated at 5 T field is 9  $\mu\text{eV}$ , which is an order of magnitude smaller than the same of the pristine perovskite, which is about  $-140 \mu\text{eV}$ . The effective  $g$ -factor for the heterostructure too is substantially smaller in magnitude than that of the corresponding parent CsPbBr<sub>3</sub> (Figure 5b). From the results, it is evident that the plasmons from Cu<sub>x</sub>S play a crucial role in the modification of the electronic structure of the hybrid. When circularly polarized light excites the LSPR modes in the presence of the magnetic field, the plasmon modes due to left and right circularly polarized light are energetically decoupled.<sup>9,12</sup> The shift in the angular frequency of LSPR is given by the expression  $\Delta\omega_c = \frac{eB}{2m^*}$ , where  $e$  is the electronic charge and  $m^*$  is the effective mass of the charge carriers. This is reflected as an extra orbital angular momentum that influences the Zeeman energy at band-edge.<sup>9</sup> While the energy space coupling between two materials requires a spectral overlap between them, the momentum space interaction can still be achieved through a transfer of momentum across the materials. Since the angular momentum is a vector quantity, the additional angular momentum coming from circular magnetoplasmonic modes can couple in multiple

configurations with the existing angular momentum at the band edge and the overall Zeeman energy could be reduced. This is consistent with the higher Urbach energy in the heterostructures and also from the earlier literature that the optical phonons supposedly play a crucial role in transferring angular momentum from plasmon band to excitonic band.<sup>9</sup>

## CONCLUSIONS

We thus studied the synthesis and structural and optical properties of a new heterostructure comprising plasmonic Cu<sub>x</sub>S and excitonic CsPbBr<sub>3</sub>, which despite having no energy overlap between two parent components can have nonresonant exciton–plasmon interaction. Detailed analysis of the structure and phase from XRD and electron microscopy revealed that the heterostructures are formed in a “cube-dot” architecture, where the dot is the plasmonic component and the cube primarily shows the excitonic component. We found that at unperturbed condition, the interaction is weak, which is supported by the higher Urbach energy associated with the excitonic band-edge and PL quenching in the heterostructures. However, under an external magnetic field, when the degeneracy of the band-edge is lifted, the interaction is strong and the excitonic band splitting is completely modified in the heterostructure from the pristine perovskite. A summary of the properties of the heterostructure along with the parent compound is shown in Table 2. To the best of our knowledge,

**Table 2. Summary of Various Physical Properties of the Heterostructure along with the Parent Components**

properties	CsPbBr <sub>3</sub>	Cu <sub>x</sub> S	Cu <sub>x</sub> S/CsPbBr <sub>3</sub>
architecture	cube	pebble	cube-dot
visible absorption (eV)	2.55	–	2.55
source	band-edge	–	band-edge
IR Absorption (eV)	–	0.73–1.77	0.73–1.77
source	–	LSPR	LSPR
PLQY	high	–	low
MCD signal	strong	–	weak, sign reversed compared to CsPbBr <sub>3</sub>
Zeeman energy at 5 T, 2 K ( $\mu\text{eV}$ )	$-140.00$	–	9.00
$g$ -factor at 2 K	1.1	–	0.08

this is the first demonstration of nonresonant exciton–plasmon interaction across two different materials and can effectively open up new possibilities in the field of plasmonics, where the magnetoplasmonic mode can be used as a new degree of freedom in photonic and optoelectronic devices.

## ASSOCIATED CONTENT

### Supporting Information

The Supporting Information is available free of charge at <https://pubs.acs.org/doi/10.1021/acs.jpcc.3c03331>.

TEM image, NIR absorbance of Cu<sub>x</sub>S, TEM image of Br-120, Cu<sub>x</sub>S/CsPbBr<sub>3</sub> HRTEM image with plane analysis, UV–visible absorption spectra of all samples washed with antisolvents, modeling of ellipsometry data, list of XAFS and ellipsometry fitting parameters, and the list of transitions in the heterostructure (PDF)

## AUTHOR INFORMATION

### Corresponding Author

Ranjani Viswanatha – New Chemistry Unit and School of Advanced Materials, Jawaharlal Nehru Centre for Advanced Scientific Research, Jakkur, Bangalore 560064, India; International Centre for Materials Science, Jawaharlal Nehru Centre for Advanced Scientific Research, Jakkur, Bangalore 560064, India; [orcid.org/0000-0002-3819-4029](https://orcid.org/0000-0002-3819-4029); Email: [rv@jncasr.ac.in](mailto:rv@jncasr.ac.in)

### Authors

Saptarshi Chakraborty – New Chemistry Unit, Jawaharlal Nehru Centre for Advanced Scientific Research, Jakkur, Bangalore 560064, India; [orcid.org/0000-0001-8559-1089](https://orcid.org/0000-0001-8559-1089)

Gauttam Dash – New Chemistry Unit, Jawaharlal Nehru Centre for Advanced Scientific Research, Jakkur, Bangalore 560064, India; [orcid.org/0000-0003-0533-9874](https://orcid.org/0000-0003-0533-9874)

Subhashri Mannar – International Centre for Materials Science, Jawaharlal Nehru Centre for Advanced Scientific Research, Jakkur, Bangalore 560064, India; [orcid.org/0000-0001-7534-704X](https://orcid.org/0000-0001-7534-704X)

Krishna Chand Maurya – Chemistry and Physics of Materials Unit, Jawaharlal Nehru Centre for Advanced Scientific Research, Jakkur, Bangalore 560064, India

Arpan Das – Theoretical Sciences Unit, Jawaharlal Nehru Centre for Advanced Scientific Research, Jakkur, Bangalore 560064, India; [orcid.org/0000-0001-9424-9170](https://orcid.org/0000-0001-9424-9170)

Shobhana Narasimhan – Theoretical Sciences Unit, Jawaharlal Nehru Centre for Advanced Scientific Research, Jakkur, Bangalore 560064, India; [orcid.org/0000-0002-1793-0576](https://orcid.org/0000-0002-1793-0576)

Bivas Saha – International Centre for Materials Science, Jawaharlal Nehru Centre for Advanced Scientific Research, Jakkur, Bangalore 560064, India; Chemistry and Physics of Materials Unit and School of Advanced Materials, Jawaharlal Nehru Centre for Advanced Scientific Research, Jakkur, Bangalore 560064, India; [orcid.org/0000-0002-0837-1506](https://orcid.org/0000-0002-0837-1506)

Complete contact information is available at:  
<https://pubs.acs.org/10.1021/acs.jpcc.3c03331>

### Notes

The authors declare no competing financial interest.

## ACKNOWLEDGMENTS

We are grateful to JNCASR for providing all the experimental and computational facilities and funding. S.C., S.M., K.C.M., A.D., and G.D. thank DST-INSPIRE, Science and Engineering Research Board (SERB), CSIR, JNCASR, and University Grants Commission respectively for research fellowships. A.D. and S.N. thank Prof. Manish Jain of IISc Bangalore for a fruitful discussion. A.D. and S.N. thank TUE-CMS, JNCASR and ParamYukti National Supercomputing Mission (NSM), JNCASR for providing excellent computational facilities. B.S. acknowledges SERB of the Government of India, Start-Up Research Grant SRG/2019/000613 for partial financial support. R.V. acknowledges a POWER-fellowship from SERB for partial financial support. XAFS measurements were carried out in P64 beamline at PETRA III of DESY, a member of the Helmholtz Association (HGF), Germany. Beamline assistance by Dr. Akhil Tayal and Dr. Wolfgang A. Caliebe is gratefully

acknowledged. Financial support by the Department of Science and Technology, Government of India, provided within the framework of India@DESY collaboration is also acknowledged.

## REFERENCES

- (1) Dibos, A. M.; Zhou, Y.; Jauregui, L. A.; Scuri, G.; Wild, D. S.; High, A. A.; Taniguchi, T.; Watanabe, K.; Lukin, M. D.; Kim, P.; et al. Electrically Tunable Exciton-Plasmon Coupling in a WSe<sub>2</sub> Monolayer Embedded in a Plasmonic Crystal Cavity. *Nano Lett.* **2019**, *19* (6), 3543–3547.
- (2) Sun, J.; Li, Y.; Hu, H.; Chen, W.; Zheng, D.; Zhang, S.; Xu, H. Strong plasmon-exciton coupling in transition metal dichalcogenides and plasmonic nanostructures. *Nanoscale* **2021**, *13* (8), 4408–4419.
- (3) Geisler, M.; Cui, X.; Wang, J.; Rindzevicius, T.; Gammelgaard, L.; Jessen, B. S.; Gonçalves, P. A. D.; Todisco, F.; Bøggild, P.; Boisen, A.; et al. Single-Crystalline Gold Nanodisks on WS<sub>2</sub> Mono- and Multilayers for Strong Coupling at Room Temperature. *ACS Photonics* **2019**, *6* (4), 994–1001.
- (4) Jiang, Y.; Wang, H.; Wen, S.; Chen, H.; Deng, S. Resonance Coupling in an Individual Gold Nanorod-Monolayer WS<sub>2</sub> Heterostructure: Photoluminescence Enhancement with Spectral Broadening. *ACS Nano* **2020**, *14* (10), 13841–13851.
- (5) Munkhbat, B.; Baranov, D. G.; Bisht, A.; Hoque, M. A.; Karpiak, B.; Dash, S. P.; Shegai, T. Electrical Control of Hybrid Monolayer Tungsten Disulfide-Plasmonic Nanoantenna Light-Matter States at Cryogenic and Room Temperatures. *ACS Nano* **2020**, *14* (1), 1196–1206.
- (6) Liu, W.; Wang, Y.; Zheng, B.; Hwang, M.; Ji, Z.; Liu, G.; Li, Z.; Sorger, V. J.; Pan, A.; Agarwal, R. Observation and Active Control of a Collective Polariton Mode and Polaritonic Band Gap in Few-Layer WS<sub>2</sub> Strongly Coupled with Plasmonic Lattices. *Nano Lett.* **2020**, *20* (1), 790–798.
- (7) Yadav, R. K.; Bourgeois, M. R.; Cherqui, C.; Juarez, X. G.; Wang, W.; Odum, T. W.; Schatz, G. C.; Basu, J. K. Room Temperature Weak-to-Strong Coupling and the Emergence of Collective Emission from Quantum Dots Coupled to Plasmonic Arrays. *ACS Nano* **2020**, *14* (6), 7347–7357.
- (8) Li, J.; Cushing, S. K.; Meng, F.; Senty, T. R.; Bristow, A. D.; Wu, N. Plasmon-induced resonance energy transfer for solar energy conversion. *Nature Photon* **2015**, *9* (9), 601–607.
- (9) Yin, P.; Tan, Y.; Fang, H.; Hegde, M.; Radovanovic, P. V. Plasmon-induced carrier polarization in semiconductor nanocrystals. *Nat. Nanotechnol.* **2018**, *13* (6), 463–467.
- (10) Yin, P.; Hegde, M.; Garnet, N. S.; Tan, Y.; Radovanovic, P. V. Faceting-Controlled Zeeman Splitting in Plasmonic TiO<sub>2</sub> Nanocrystals. *Nano Lett.* **2019**, *19* (9), 6695–6702.
- (11) Yin, P.; Tan, Y.; Ward, M. J.; Hegde, M.; Radovanovic, P. V. Effect of Dopant Activation and Plasmon Damping on Carrier Polarization in In<sub>2</sub>O<sub>3</sub> Nanocrystals. *J. Phys. Chem. C* **2019**, *123* (49), 29829–29837.
- (12) Yin, P.; Chen, S.; Radovanovic, P. V. Properties of Free Charge Carriers Govern Exciton Polarization in Plasmonic Semiconductor Nanocrystals. *J. Phys. Chem. Lett.* **2022**, *13* (24), 5545–5552.
- (13) Han, B.; Gao, X.; Lv, J.; Tang, Z. Magnetic Circular Dichroism in Nanomaterials: New Opportunity in Understanding and Modulation of Excitonic and Plasmonic Resonances. *Adv. Mater.* **2020**, *32* (41), 1801491.
- (14) Chakraborty, S.; Mannar, S.; Viswanatha, R. Local Surface Plasmon-Assisted Metal Oxide Perovskite Heterostructure for Small Light Emitters. *J. Phys. Chem. C* **2021**, *125* (19), 10565–10571.
- (15) Protesescu, L.; Yakunin, S.; Bodnarchuk, M. I.; Krieg, F.; Caputo, R.; Hendon, C. H.; Yang, R. X.; Walsh, A.; Kovalenko, M. V. Nanocrystals of Cesium Lead Halide Perovskites (CsPbX<sub>3</sub>, X = Cl, Br, and I): Novel Optoelectronic Materials Showing Bright Emission with Wide Color Gamut. *Nano Lett.* **2015**, *15* (6), 3692–3696.
- (16) Jain, A.; Ong, S. P.; Hautier, G.; Chen, W.; Richards, W. D.; Dacek, S.; Cholia, S.; Gunter, D.; Skinner, D.; Ceder, G.; et al.

Commentary: The Materials Project: A materials genome approach to accelerating materials innovation. *APL Mater.* **2013**, *1* (1), 011002.

(17) Ravel, B.; Newville, M. ATHENA, ARTEMIS, HEPHAESTUS: data analysis for X-ray absorption spectroscopy using IFEFFIT. *J. Synchrotron Rad.* **2005**, *12* (4), 537–541.

(18) Giannozzi, P.; Baroni, S.; Bonini, N.; Calandra, M.; Car, R.; Cavazzoni, C.; Ceresoli, D.; Chiarotti, G. L.; Cococcioni, M.; Dabo, I.; et al. QUANTUM ESPRESSO: a modular and open-source software project for quantum simulations of materials. *J. Phys.: Condens. Matter* **2009**, *21* (39), 395502.

(19) Hamann, D. R. Optimized norm-conserving Vanderbilt pseudopotentials. *Phys. Rev. B* **2013**, *88* (8), 085117.

(20) Perdew, J. P.; Burke, K.; Ernzerhof, M. Generalized Gradient Approximation Made Simple. *Phys. Rev. Lett.* **1996**, *77* (18), 3865–3868.

(21) Monkhorst, H. J.; Pack, J. D. Special points for Brillouin-zone integrations. *Phys. Rev. B* **1976**, *13* (12), 5188–5192.

(22) Marzari, N.; Vanderbilt, D.; De Vita, A.; Payne, M. C. Thermal Contraction and Disorder of the Al(110) Surface. *Phys. Rev. Lett.* **1999**, *82* (16), 3296–3299.

(23) Ehrenreich, H.; Philipp, H. R. Optical Properties of Ag and Cu. *Phys. Rev.* **1962**, *128* (4), 1622–1629.

(24) Hu, C.; Chen, W.; Xie, Y.; Verma, S. K.; Destro, P.; Zhan, G.; Chen, X.; Zhao, X.; Schuck, P. J.; Kriegel, I.; et al. Generating plasmonic heterostructures by cation exchange and redox reactions of covellite CuS nanocrystals with Au<sup>3+</sup> ions. *Nanoscale* **2018**, *10* (6), 2781–2789.

(25) Zhang, X.; Wu, X.; Liu, X.; Chen, G.; Wang, Y.; Bao, J.; Xu, X.; Liu, X.; Zhang, Q.; Yu, K.; et al. Heterostructural CsPbX<sub>3</sub>-PbS (X = Cl, Br, I) Quantum Dots with Tunable Vis-NIR Dual Emission. *J. Am. Chem. Soc.* **2020**, *142* (9), 4464–4471.

(26) Dang, Z.; Shamsi, J.; Palazon, F.; Imran, M.; Akkerman, Q. A.; Park, S.; Bertoni, G.; Prato, M.; Brescia, R.; Manna, L. In Situ Transmission Electron Microscopy Study of Electron Beam-Induced Transformations in Colloidal Cesium Lead Halide Perovskite Nanocrystals. *ACS Nano* **2017**, *11* (2), 2124–2132.

(27) Erslev, P. T.; Chen, H.-Y.; Gao, J.; Beard, M. C.; Frank, A. J.; van de Lagemaat, J.; Johnson, J. C.; Luther, J. M. Sharp exponential band tails in highly disordered lead sulfide quantum dot arrays. *Phys. Rev. B* **2012**, *86* (15), 155313.

(28) Kostadinov, I. Z. The Urbach tail in amorphous semiconductors. *J. Phys. C: Solid State Phys.* **1977**, *10* (9), L263–L266.

(29) Urbach, F. The Long-Wavelength Edge of Photographic Sensitivity and of the Electronic Absorption of Solids. *Phys. Rev.* **1953**, *92* (5), 1324–1324.

(30) Yang, D.; Li, X.; Wu, Y.; Wei, C.; Qin, Z.; Zhang, C.; Sun, Z.; Li, Y.; Wang, Y.; Zeng, H. Surface Halogen Compensation for Robust Performance Enhancements of CsPbX<sub>3</sub> Perovskite Quantum Dots. *Adv. Opt. Mater.* **2019**, *7* (11), 1900276.

(31) Dow, J. D.; Redfield, D. Toward a Unified Theory of Urbach's Rule and Exponential Absorption Edges. *Phys. Rev. B* **1972**, *5* (2), 594–610.

(32) De Wolf, S.; Holovsky, J.; Moon, S.-J.; Löper, P.; Niesen, B.; Ledinsky, M.; Haug, F.-J.; Yum, J.-H.; Ballif, C. Organometallic Halide Perovskites: Sharp Optical Absorption Edge and Its Relation to Photovoltaic Performance. *J. Phys. Chem. Lett.* **2014**, *5* (6), 1035–1039.

(33) Chen, S.; Lyu, D.; Ling, T.; Guo, W. Reversible modulation of CsPbBr<sub>3</sub> perovskite nanocrystal/gold nanoparticle heterostructures. *Chem. Commun.* **2018**, *54* (36), 4605–4608.

(34) Roman, B. J.; Otto, J.; Galik, C.; Downing, R.; Sheldon, M. Au Exchange or Au Deposition: Dual Reaction Pathways in Au-CsPbBr<sub>3</sub> Heterostructure Nanoparticles. *Nano Lett.* **2017**, *17* (9), 5561–5566.

(35) Chen, K.; Wang, Y.; Liu, J.; Kang, J.; Ge, Y.; Huang, W.; Lin, Z.; Guo, Z.; Zhang, Y.; Zhang, H. In situ preparation of a CsPbBr<sub>3</sub>/black phosphorus heterostructure with an optimized interface and photo-detector application. *Nanoscale* **2019**, *11* (36), 16852–16859.

(36) Fan, C.; Xu, X.; Yang, K.; Jiang, F.; Wang, S.; Zhang, Q. Controllable Epitaxial Growth of Core-Shell PbSe@CsPbBr<sub>3</sub> Wire Heterostructures. *Adv. Mater.* **2018**, *30* (45), 1804707.

(37) Zhao, M.; Shi, Y.; Dai, J.; Lian, J. Ellipsometric study of the complex optical constants of a CsPbBr<sub>3</sub> perovskite thin film. *J. Mater. Chem. C* **2018**, *6* (39), 10450–10455.

(38) Bailey, C. G.; Piana, G. M.; Lagoudakis, P. G. High-Energy Optical Transitions and Optical Constants of CH<sub>3</sub>NH<sub>3</sub>PbI<sub>3</sub> Measured by Spectroscopic Ellipsometry and Spectrophotometry. *J. Phys. Chem. C* **2019**, *123* (47), 28795–28801.

(39) Chen, X.; Wang, Y.; Song, J.; Li, X.; Xu, J.; Zeng, H.; Sun, H. Temperature Dependent Reflectance and Ellipsometry Studies on a CsPbBr<sub>3</sub> Single Crystal. *J. Phys. Chem. C* **2019**, *123* (16), 10564–10570.

(40) Akkerman, Q. A.; Nguyen, T. P. T.; Boehme, S. C.; Montanarella, F.; Dirin, D. N.; Wechsler, P.; Beiglböck, F.; Rainò, G.; Erni, R.; Katan, C.; et al. Controlling the nucleation and growth kinetics of lead halide perovskite quantum dots. *Science* **2022**, *377* (6613), 1406–1412.

(41) Jacoby, L. M.; Crane, M. J.; Gamelin, D. R. Coherent Spin Dynamics in Vapor-Deposited CsPbBr<sub>3</sub> Perovskite Thin Films. *Chem. Mater.* **2022**, *34* (4), 1937–1945.